JACS
JOURNAL OF THE AMERICAN CHEMICAL SOCIETY

COMMUNICATION

pubs.acs.org/JACS

Raman Analysis of Mode Softening in Nanoparticle $CeO_{2-\delta}$ and Au-$CeO_{2-\delta}$ during CO Oxidation

Youjin Lee,[†] Guanghui He,[†] Austin J. Akey,[†] Rui Si,[‡] Maria Flytzani-Stephanopoulos,[‡] and Irving P. Herman*[,†]

[†]Department of Applied Physics and Applied Mathematics, Columbia University, New York, New York 10027, United States

[‡]Department of Chemical and Biological Engineering, Tufts University, Medford, Massachusetts 02155, United States

Supporting Information

ABSTRACT: Oxygen vacancy levels are monitored during the oxidation of CO by $CeO_{2-\delta}$ nanorods and Au-$CeO_{2-\delta}$ nanorods, nanocubes, and nanopolyhedra by using Raman scattering. The first-order CeO_2 F_{2g} peak near 460 cm^{-1} decreases when this reaction is fast (fast reduction and relatively slow reoxidation of the surface), because of the lattice expansion that occurs when Ce^{3+} replaces Ce^{4+} during oxygen vacancy creation. This shift correlates with reactivity for CO oxidation. Increases in the oxygen deficit δ as large as ~0.04 are measured relative to conditions when the ceria is not reduced.

CeO_2 (cerium oxide, ceria, $CeO_{2-\delta}$) is widely used as a catalyst that can assist in storing and releasing oxygen.[1,2] The reactive and catalytic properties of CeO_2 are superior in nanoparticle form because of the larger surface area and a change in structure and composition due to oxygen vacancies.[3] Catalytic activity is enhanced when gold is deposited on the nanoparticle surface, Au-CeO_2, and depends on CeO_2 particle size and shape.[4−10] For example, the water−gas shift reaction is faster for nanorods (with exposed {110} and {100} CeO_2 surface planes) than for nanopolyhedra ({111} and {100}), which is much faster than that for nanocubes ({100}).[10] One fundamental impediment to understanding the reactivity of catalysts has been characterizing them in real time. In particular, analyzing oxygen vacancy levels in ceria in real time during such catalytic-type reactions has been a challenge, a challenge that is successfully addressed here.

Raman scattering is an intriguing tool for monitoring and understanding the catalytic activity of ceria. For example, the strength of the Raman peak near 570 cm^{-1} relative to that of the first-order F_{2g} peak in CeO_2 near 460 cm^{-1} has been associated with oxygen vacancies in CeO_2 and cation-doped CeO_2.[11−18] The feature provides mechanistic insight, but the use of the strength of this peak to assess vacancy concentration quantitatively is limited by its multipeak nature,[12] and uncertainty of how the integrated feature strength varies with defect density and whether it varies monotonically with vacancy density.[15] Using UV Raman scattering,[19] ref 12 showed that the relative density of defect sites (~595 cm^{-1}) on oxidized surfaces of nanoparticle CeO_2 varies as nanorods > nanocubes > nano-octahedra; these intrinsic defects may be Frenkel-type oxygen defects. On reduced ceria, the defect peak moves from 592 cm^{-1} to ~560 cm^{-1} and becomes weaker relative to the F_{2g} peak; these changes are reversed when O_2 is added, so the lower energy peak is thought to be due to oxygen vacancies. The first-order F_{2g} peak shift in CeO_2 is known to decrease when either particle size decreases or temperature increases (in the presence of air);[20] however, no connection between this Raman scattering peak, CeO_2 catalytic activity, and oxygen vacancies has been noted.

In this communication, we report that the F_{2g} Raman peak shifts in $CeO_{2-\delta}$ and Au-$CeO_{2-\delta}$ nanoparticles of certain shapes decrease during the oxidation of CO more than would be expected from thermal expansion and phonon decay. These additional decreases are quantitatively related to increases in oxygen vacancies (the oxygen deficit δ) that accompany CO oxidation.

CeO_2 and Au-CeO_2 nanoparticles were synthesized as previously reported in ref 10. Different ceria particle shapes (nanorods, nanocubes, nanopolyhedra) were prepared by varying the synthesis conditions. Only the face-centered cubic (fcc) structure of CeO_2 (space group: Fm3m) is observed in powder X-ray diffraction, without any isolated Au phase from each sample. Using transmission electron microscopy TEM, the average CeO_2 particle dimensions are: (10.1 ± 2.8) × (50−200) nm for rods, 29.5 ± 10.6 nm for cubes, and 11.0 ± 2.1 nm for polyhedra. Gold was then introduced to calcined (400 °C, air) ceria nanoshapes by deposition-precipitation (DP) to produce Au-CeO_2. The three different-shaped ceria nanoparticles are seen to maintain their original crystal shapes after gold deposition. X-ray photoelectron spectroscopy (XPS) and inductively coupled plasma atomic emission spectroscopy (ICP-AES) suggest that the introduced Au (~1% atomic concentration) remains mostly on the surface or the subsurface layers of CeO_2.[10] XPS also shows that ionic gold (Au^+ and Au^{3+}) is the main species on the rod and polyhedron samples, while metallic gold (Au^0) is dominant on the cubes. TEM suggests that the gold is in the form of particles only on the nanocubes. More details about sample preparation and properties can be found in ref 10. Bulk CeO_2 (average particle size ~5 μm, Alfa Aesar, 99.9%) was also used.

About 10 mg of a given powder sample was placed on a temperature-controlled Si wafer substrate in a flow cell (Linkam THMS 600 thermal stage). Raman analysis of each sample was conducted in this cell with gas flowing (20 sccm, ~1 atm) "over"

Received: May 20, 2011
Published: July 22, 2011

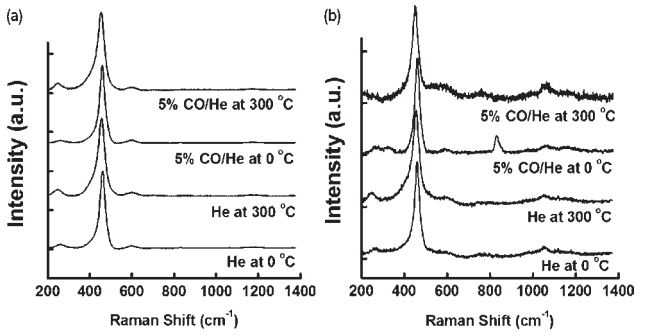

Figure 1. Raman spectra of (a) CeO_2 and (b) Au-CeO_2 nanorods with 5% CO/He and He flow.

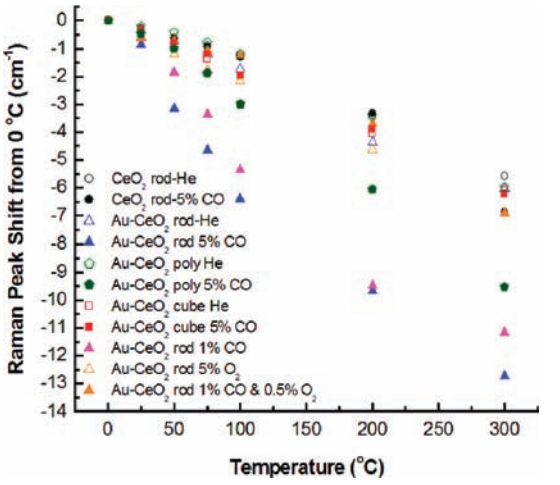

Figure 2. Main CeO_2 Raman peak (F_{2g}) shifts (relative to the shifts at 0 °C) as a function of temperature during flow over CeO_2 nanorods, Au-CeO_2 nanorods, Au-CeO_2 nanopolyhedra, and Au-CeO_2 nanocubes. CO indicates 5% CO, 1% CO, and 1% CO/0.5% O_2 flows that are in He, and O_2 indicates 5% O_2/N_2 flow.

the powder and residual gas analysis (RGA) was performed on the effluent from this cell. Raman analysis was performed using 514 nm excitation from an argon-ion laser, and analysis by a spectrometer with an 1800 groove/mm grating blazed at 500 nm (Acton SPi2300, Princeton Instruments) and a liquid nitrogen-cooled CCD detector (SPEC-10, Princeton Instruments). Raman peak shifts were determined by fitting with Lorentzian lineshapes ($R^2 > 0.95$). RGA analysis was conducted in the cell effluent when CO was flowed, using a Balzers-Pfeiffer model PRISMA QME 200. Mass 44 peaks from CO oxidation product CO_2 were referenced to the mass 4 He peak in the flowing CO/He gas mixture.

In most studies, the flowing gas was He, 5% CO/He, or 5% O_2/N_2. Before each run, He was flowed for 30 min with the sample held at 350 °C, and then cooled to 0 °C. Raman and RGA measurements were conducted with the substrate temperature ramped from 0 to 300 at 50 °C/min between selected temperatures (0, 25, 50, 75, 100, 200, and 300 °C) with the substrate maintained at each temperature for 10 min: 5 min for temperature stabilization, followed by 5 min for Raman analysis. Each run was conducted with a fresh sample.

At 0 °C, CO_2 is detected in the effluent during 5% CO/He flow over Au-CeO_2 rods and polyhedra, but not during flow over CeO_2 rods or Au-CeO_2 cubes. CO_2 product by CeO_2 rods is negligible below 100 °C, and is always much smaller than for Au-CeO_2 rods at the same temperature. At 300 °C, the CO conversion with 5% CO/He flow over Au-CeO_2 rods is ~2.5× that over CeO_2 rods, ~1.7× that over Au-CeO_2 polyhedra, and ~5× that over Au-CeO_2 cubes. (See Figures S1 and S2 in Supporting Information [SI] for more on the RGA results.)

Figure 1 shows the Raman spectra of CeO_2 and Au-CeO_2 rods at 0 and 300 °C for He and 5% CO/He gas flows, presented normalized to the peak height of the CeO_2 F_{2g} peak near 460 cm^{-1}. (See Figure S3 in SI for more details on the Raman spectra.) There is a small variation in the F_{2g} mode Raman shifts of the different samples at 0 °C, with those for CeO_2 and Au-CeO_2 rods being ~460 cm^{-1} (with the Au-CeO_2 peak about 0.8−1.4 cm^{-1} higher than that for CeO_2) and those for Au-CeO_2 cubes and polyhedra being ~464 cm^{-1}. Smaller peaks near 260, 600, 760, 830, and 1050 cm^{-1} also depend on temperature and reaction conditions. (See SI.)

The peak shifts of the F_{2g} mode vs temperature are plotted for the different gas flows over different samples in Figure 2, offset to coincide at 0 °C for each run so the changes (decreases) in Raman shifts with increasing temperatures are seen. The decreases in the Raman shifts from 0 to 300 °C range from ~6 to ~13 cm^{-1}. The examples with this ~6 cm^{-1} change include all 5% CO/He, He, and 5% O_2/N_2 runs with bulk CeO_2 and Au-CeO_2 nanocubes, and all runs with 5% O_2/N_2 flow (for these and for CeO_2 rods, and Au-CeO_2 rods and polyhedra). The largest shifts are seen for 5% CO/He flow, for CeO_2 rods and for Au-CeO_2 rods and polyhedra, with the largest of all being for Au-CeO_2 rods. For these three samples, the decrease in Raman shift is much larger with 5% CO/He flow than with either He or 5% O_2/N_2 flow, and slightly larger with He flow than with 5% O_2/N_2 flow. In all cases this Raman shift change is largely reversible as the temperature is decreased, as shown in Figure S3 in the SI.

The decrease in Raman shift by ~6 cm^{-1} from 0 to 300 °C seen in many cases is due only to thermal expansion and phonon coupling and decay; this is similar to that seen by ref 20 for bulk and CeO_2 nanoparticles in air. The additional downward shift seen in several cases is mostly due to the lattice expansion and mode softening that occurs when oxygen vacancies are created (from the oxidation of CO or potentially other mechanisms), which leads to two Ce^{3+} ions (ionic radius 1.143 Å) replacing two Ce^{4+} ions (0.970 Å) for each oxygen vacancy created.[21−23]

The largest downshifts are seen during 5% CO/He flow whenever there is significant CO_2 product (CeO_2 rods, Au-CeO_2 rods and polyhedra), as monitored by RGA, for a given sample type and temperature; the largest reaction yields in these cases correlate with the largest changes in Raman shifts. The reaction yield and extra decrease in Raman shift both occur continuously from 0 to 300 °C for Au-CeO_2 rods, but they both become noticeable only near 300 °C for CeO_2 rods. In each case, the larger downshifts are seen when the oxygen vacancy levels are expected to be high because of the relatively rapid ceria reduction during CO oxidation and the very slow regeneration of surface and bulk oxygen vacancies.

For Au-CeO_2 rods at 300 °C, the CO_2 product is ~2× larger during 1% CO/0.5% O_2/He flow than during 5% CO/He flow, which is itself ~2× than that during 1% CO/He flow. (In the absence of the powder, no CO_2 product is seen with 1% CO/0.5% O_2/He flow at 300 °C.) However, the Raman shift decrease with 1% CO/0.5% O_2/He flow is only ~0.01 cm^{-1} (relative to that with 5% O_2/N_2) (compared to 5.8 and 4.3 cm^{-1} for 5%

dx.doi.org/10.1021/ja204479j |J. Am. Chem. Soc. 2011, 133, 12952–12955

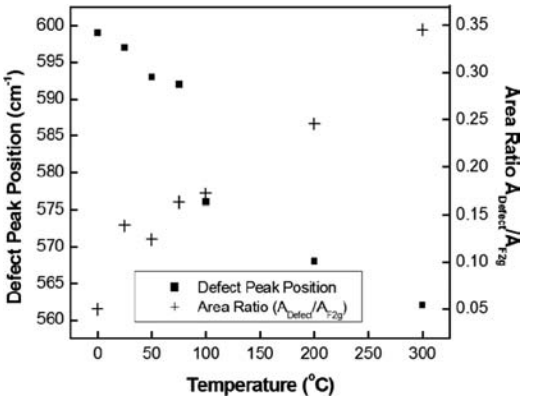

Figure 3. Raman shift of the defect peak near 570 cm^{-1} and the integrated area of this peak (normalized by that of the F_{2g} peak) for Au-CeO_2 nanorods with 5% CO/He flow vs temperature.

CO/He and 1% CO/He flow, respectively) (Figure 2). The respective values relative to those with He flow are 0.90, 6.7, and 5.1 cm^{-1}. RGA traces in Figure S2 (in SI) show evidence of CO oxidation by Au-CeO_2 rods during 5% CO/He flow: from trace O_2, starting at the lowest temperatures due to oxidation by O_2 (with no slowing of this rate with time because there is no loss of lattice oxygen), from ceria lattice oxygen, starting at higher temperatures (with the oxidation rate slowing with time due to loss of lattice oxygen), and from trace water vapor (through the water−gas shift reaction) at the highest temperatures; with 1% CO/0.5% O_2/He flow, there is evidence of only CO oxidation due to the O_2 flow. This confirms the attribution of the larger changes in Raman shifts to volume changes arising from oxygen vacancies.

The decrease in the F_{2g} mode shift of Au-CeO_2 nanorods in 5% CO/He flow from 0 to 300 °C (relative to the shift at 0 °C) in Figure 2 (blue triangles) is similar to the general decrease of the defect mode shift (from 599 to 562 cm^{-1}) and the general increase of the ratio of the areas of this defect peak to that of the F_{2g} mode (from 0.05 to 0.34) seen in Figure 3 for the same runs. Ref 12 has shown that the defect peak includes contributions from intrinsic defects and oxygen vacancies. This further reinforces the association of the changes in the F_{2g} mode shift with vacancies.

At 300 °C, the F_{2g} Raman shift is lower with 5% CO/He flow than with 5% O_2/N_2 flow by 5.8, 3.1, 0.28, and 0.96 cm^{-1} for Au-CeO_2 rods, polyhedra, and cubes and CeO_2 rods respectively, and this downshift is usually even lower for He flow, and is 6.7, 3.6, 0.15, and 1.3 cm^{-1}, respectively. These are $-\Delta\omega$ relative to the reference frequency ω with the reference flow, and represent the average of two runs with very similar results. For bulk CeO_2, the Raman shifts with 5% O_2/N_2 and He flows are the same within 0.1 cm^{-1}.

This additional downshift with CO flow, is $\Delta\omega = -\gamma\omega(\Delta V/V_0)$, where γ is the Grüneisen parameter for this mode (1.24, assumed to be independent of temperature[11]), and ΔV is the volume change from the reference case volume V_0. This fractional volume change of $CeO_{2-\delta}$ is due to the consequences of the oxygen vacancies leading to the oxygen deficit δ: expansion due to the change of Ce^{4+} (ionic radius 0.970 Å) to Ce^{3+} (1.143 Å), which is partially offset by the effective compression due to the loss of O^{2-} (1.380 Å) and the creation of oxygen vacancies (1.164 Å).[22] Even when the contribution of intrinsic vacancy trimers is included,[23] the relation between δ and V/V_0 is largely linear, with $\delta = -10(\Delta a/a_0) = -3.3(\Delta V/V_0)$, where $\Delta a/a_0$ (assumed to be $\ll 1$) is the fractional change in lattice constant. The oxygen deficit is then $\delta = 2.66(\Delta\omega/\omega)$.

Using the Raman shift values at 300 °C, for 5% CO/He flow the increase in oxygen deficit (relative to that with 5% O_2/N_2 flow) at this temperature is $\delta = 0.034$ for Au-CeO_2 rods, 0.018 for Au-CeO_2 polyhedra, 0.0016 for Au-CeO_2 cubes, and 0.0056 for CeO_2 rods, and 0.039, 0.021, 0.0009, and 0.0076, respectively, relative to He flow. For the estimated ±0.3 cm^{-1} uncertainty in $\Delta\omega/\omega$, the uncertainty in δ is ±0.002. With 1% CO/He and 1% CO/0.5% O_2/He flow over Au-CeO_2 rods, the increases in δ are respectively 0.025 and 0.0001 relative to those (very small values) for 5% O_2/N_2, and 0.030 and 0.005 relative to those (very small values) for He flow.

Larger decreases in the Raman shift indicate more vacancies, due to faster reaction with relatively slow surface reoxidation (as for 5% CO/He flow over Au-CeO_2 rods and polyhedra and CeO_2 rods), while smaller shifts indicate slower reaction (5% CO/He flow over CeO_2 rods or Au-CeO_2 cubes) or fast reaction with fast surface reoxidation or little net oxygen vacancy creation (1% CO/0.5% O_2/He flow over Au-CeO_2 rods). Vacancy levels and reactivity are both very sensitive to nanoparticle shape, exposed surfaces, and the presence of Au.

Uncertainties in this quantitative analysis include how oxygen vacancies at and near the surface in nanoparticles affect volume expansion and the measured Raman spectrum differently than those in the bulk. Also, ref 11 suggests very small mode hardening of the CeO_2 F_{2g} mode (up to 1−2 cm^{-1} for up to $\delta = 0.2$ in bulk ceria) when oxygen vacancies are introduced (with no other effects included, such as volume expansion). Another effect excluded is the change in force constants due to the "alloying" with Ce^{3+}. In addition, the smaller F_{2g} mode frequency at 0 °C for nanorods (~460 cm^{-1}) than for nanocubes, nanopolyhedra, and the bulk (~464 cm^{-1}) could indicate different surface or bulk effects for different particles. However, each of these factors is expected to be small relative to the large shift decrease with 5% CO/He flow and the effects of thermal expansion and phonon decay. There is uncertainty in the Grüneisen parameter of the ceria F_{2g} mode. Use of γ =1.44 (instead of 1.24)[11] would decrease the determined oxygen deficit by 14%, so the largest value determined here would be 0.034 instead of 0.039. Another uncertainty involves the Raman probing of an inhomogeneous set of particles. Within the Raman probe depth, the reduction of particles near the top of the sample on the substrate should be more complete, and consequently the oxygen deficits in these particles would be larger than those in the deeper regions. This may affect the details of the quantitative analysis to a small degree.

Figure 4 plots how the magnitude of the downshift of the F_{2g} Raman mode varies with the CO_2 product formed (relative to that with He flow), for each run with CO flow and for each temperature in that run. There is a general increase in Raman downshift (and consequently oxygen vacancies) with CO_2 product except for runs with relatively little CO_2 produced and for runs with O_2 flow as well as CO flow. The points are off the main plot in these latter runs, because surface oxidation of CO is due to the O_2 flow, and lattice oxygen is not consumed. The initial toe in Figure 4, where negligible Raman shift is observed even with the increase in the CO_2 product, is attributed to CO oxidation by trace impurity O_2, along with negligible net oxygen vacancy creation. Increased CO_2 product correlates with the CO reduction of the surface (creation of oxygen vacancies), causing

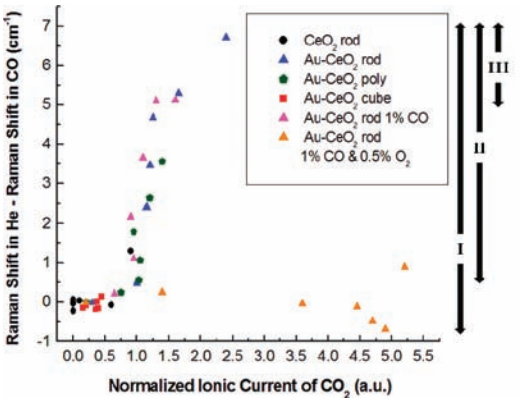

Figure 4. Downshift of the CeO_2 Raman peak (F_{2g}) shift is plotted vs the normalized RGA current at mass 44 (single ionized CO_2) for all runs with CO flow. Each data point represents the difference of the Raman shift with He flow relative to that for the same material with the specified flow at each temperature chosen from 0 to 300 °C. (This difference is corrected for the differences at 0 °C, as in Figure 2.) The gas flow is 5% CO/He unless otherwise noted. The 1% CO and 1% CO/0.5% O_2 flows are in He. The RGA data are taken 5 min after the specific temperature is reached, at the beginning of the 5 min Raman signal integration. The points far off the main curves are for 1% CO/0.5% O_2/He flow over Au-CeO_2 nanorods. Also shown are the ranges of the three major reaction pathways of CO oxidation on the surface: (I) the gas phase reaction CO (g) + 1/2 O_2 (g) → CO_2 (g); (II) oxidation by lattice oxygen of CeO_2; and (III) the water−gas shift reaction (CO + H_2O → CO_2 + H_2). (See SI.)

larger downshifts in the Raman shift. When the water−gas shift reaction becomes important (here at higher temperatures, and due to trace water vapor), there is even larger CO_2 product, and oxygen vacancies increase, but perhaps a little slower due to surface oxidation by the trace water vapor. (The detailed reaction mechanisms are discussed in the SI (Figure S2).) While this plot is instructive, note the plotted variables denote different time periods and locations probed on the particle (surface, subsurface, bulk). The RGA signal describes the current rate of CO oxidation either by surface reduction (lattice oxygen) or external oxygen sources (O_2 or H_2O), while the Raman shift change described by the concentrations of oxygen vacancies on the surface and in the bulk, depends on the history of net vacancy creation from surface reduction and reoxidation.

In summary, Raman analysis of phonon softening provides a direct and versatile way of quantitatively assessing oxygen vacancy levels in catalyst-type material. The rates of CO oxidation and ceria reduction correlate to the Raman shift and the increase in the oxygen deficit. The different reaction pathways of CO oxidation are confirmed both by oxygen vacancy levels from the Raman shift and by RGA analysis. In addition to being more reactive, Au-CeO_2 nanorods are seen by Raman analysis to have larger oxygen vacancy levels during CO oxidation than Au-CeO_2 nanoparticles of other shapes and CeO_2 nanorods. More extensive studies of Raman analysis of Au-CeO_2 nanoparticles during catalysis are underway.

■ ASSOCIATED CONTENT

Supporting Information. Additional experimental results in residual gas analysis and Raman scattering. This material is available free of charge via the Internet at http://pubs.acs.org.

■ AUTHOR INFORMATION

Corresponding Author
iph1@columbia.edu

■ ACKNOWLEDGMENT

We thank Wei Wang, Sarbajit Banerjee, and Dae In Kim for early contributions related to this study. This work was supported by DoE DE-FG02-05ER15730.

■ REFERENCES

(1) Yao, H. C.; Yu Yao, Y. F. *J. Catal.* **1984**, *86*, 254.
(2) Mogensen, M.; Sammes, N. M.; Tompsett, G. A. *Solid State Ionics* **2000**, *129*, 63.
(3) Zhang, F.; Chan, S.-W.; Spanier, J. E.; Apak, E.; Jin, Q.; Robinson, R. D.; Herman, I. P. *Appl. Phys. Lett.* **2002**, *80*, 127.
(4) Fu, Q.; Weber, A.; Flytzani-Stephanopoulos, M. *Catal. Lett.* **2001**, *77*, 87.
(5) Yi, N.; Si, R.; Saltsburg, H.; Flytzani-Stephanopoulos, M. *Energy Environ. Sci.* **2010**, *3*, 831.
(6) Fu, Q.; Deng, W.; Saltsburg, H.; Flytzani-Stephanopoulos, M. *Appl. Catal., B* **2005**, *56*, 57.
(7) Fu, Q.; Saltsburg, H.; Flytzani-Stephanopoulos, M. *Science* **2003**, *301*, 935.
(8) Carrettin, S.; Concepción, P.; Corma, A.; López Nieto, J. M.; Puntes, V. F. *Angew. Chem., Int. Ed.* **2004**, *43*, 2538.
(9) Fierro-Gonzalez, J. C.; Gates, B. C. *Catal. Today* **2007**, *122*, 201.
(10) Si, R.; Flytzani-Stephanopoulos, M. *Angew. Chem., Int. Ed.* **2008**, *47*, 2884.
(11) McBride, J. R.; Hass, K. C.; Poindexter, B. D.; Weber, W. H. *J. Appl. Phys.* **1994**, *76*, 2435.
(12) Wu, Z.; Li, M.; Howe, J.; Meyer, H. M., III; Overbury, S. H. *Langmuir* **2010**, *26*, 16595.
(13) Pu, Z.-Y.; Liu, X. S.; Jia, A. P.; Xie, Y. L.; Lu, J. Q.; Luo, M.-F. *J. Phys. Chem. C* **2008**, *112*, 15045.
(14) Taniguchi, T.; Watanabe, T.; Sugiyama, N.; Subramani, A. K.; Wagata, H.; Matsushita, N.; Yoshimura, M. *J. Phys. Chem. C* **2009**, *113*, 19789.
(15) Nakajima, A.; Yoshihara, A.; Ishigame, M. *Phys. Rev. B* **1994**, *50*, 13297.
(16) Dohčević-Mitrović, Z.; Popović, Z. V.; Šćepanović, M. *Acta Phys. Pol., A* **2009**, *116*, 36.
(17) Pushkarev, V. V.; Kovalchuk, V. I.; d'Itri, J. L. *J. Phys. Chem. B* **2004**, *108*, 5341.
(18) Lin, W.; Herzing, A. A.; Kiely, C. J.; Wachs, I. E. *J. Phys. Chem. C* **2008**, *112*, 5942.
(19) Stair, P. C.; Li, C. *J. Vac. Sci. Technol., A* **1997**, *15*, 1679.
(20) Spanier, J. E.; Robinson, R. D.; Zhang, F.; Chan, S.-W.; Herman, I. P. *Phys. Rev. B* **2001**, *64*, 245407.
(21) Kim, D.-J. *J. Am. Ceram. Soc.* **1989**, *72*, 1415.
(22) Hong, S. J.; Virkar, A. V. *J. Am. Ceram. Soc.* **1995**, *78*, 433.
(23) Bishop, S. R.; Duncan, K. L.; Wachsman, E. D. *Electrochim. Acta* **2009**, *54*, 1436.